Understanding nanomechanical and surface ellipsometry of optical F-doped SnO2 thin films by in-line APCVD

Afzaal, M, Yates, HM, Al-Ahmed, A, Ul-Hamid, A, Salhi, B and Ali, M

http://dx.doi.org/10.1007/s00339-020-04033-z

Understanding nanomechanical and surface ellipsometry of optical F-doped SnO_2 thin films by in-line APCVD

Mohammad Afzaal,*[1] Heather M. Yates,[2] Amir Al-Ahmed,[3] Anwar Ul-Hamid,[4] Billel Salhi,[5] and Murad Ali[6]

[1]Maths and Natural Sciences Division, Higher Colleges of Technology, Sharjah, United Arab Emirates. E-mail: mafzaal@hct.ac.ae

[2]Materials and Physics Research Centre, University of Salford, Manchester, M5 4WT, United Kingdom

[3]Center of Research Excellence in Renewable Energy, King Fahd University of Petroleum & Minerals, Dhahran-31261, Kingdom of Saudi Arabia

[4]Center for Engineering Research, Research Institute, King Fahd University of Petroleum & Minerals, Dhahran-31261, Kingdom of Saudi Arabia

[5]Center for environment and water, King Fahd University of Petroleum & Minerals, Dhahran-31261, Kingdom of Saudi Arabia

[6]Department of Mechanical Engineering, Khalifa University of Science and Technology, Main Campus, Abu Dhabi 127788, United Arab Emirates

Abstract

In this paper, a production-type chemical vapour deposition (CVD) is utilized to deposit fluorine doped tin oxide thin films of different thicknesses and dopant levels. Deposited films showed a preferred orientation along the (200) plane of a tetragonal structure due to the formation of halogen rich polar molecules during the process. A holistic approach studying elastic modulus and hardness of resulting films by a high-throughput atmospheric-pressure CVD process is described. The hardness values determined lie between 8 - 20 GPa. For a given load, the modulus generally increased slightly with the thickness. The average elastic recovery for the coatings was found to be between 45 – 50 %. Refractive index and thickness values derived from the fitted ellipsometry data were in excellent agreement with independent calculations from transmission and reflection data.

Keywords: chemical vapor deposition; tin oxide; refractive index; nanoindentation; ellipsometer

1 Introduction

Fluorine-doped tin oxide (FTO) thin films have become a major choice of transparent conducting oxide (TCO) material from the point of both energy capture and conservation. These combine high transparency in the visible region, increased electrical conductivity, along with reduced material costs, and improved thermal and chemical stabilities over TCO's such as indium tin oxide [1]. The improved stabilities of FTO's, over other TCO's such as indium tin oxide, are related to the large grain sizes at high deposition temperatures along with formation of ionic Sn-F bond. These attributes have provided much impetus into the use of FTO substrates for diverse technologies such as photovoltaic applications, [2] low emissivity windows, [3] touch screen displays, [4] and light-emitting diodes [5].

Large-scale industrial production of FTOs is usually carried out using chemical vapour deposition (CVD) at atmospheric pressure (AP) as it has the ability to deposit thin films with accelerated deposition rates, high production volumes, good process chemical stability, and low operating costs. One such example is TEC 7 produced by NSG using an in-line CVD process [6]. Extensive literature exists on the electrical and optical properties of FTOs, which can be effectively tailored by controlling deposition parameters, for example, flow rates, temperatures, precursor ratios, susceptor translation rates and dopant levels [7]. On the contrary, mechanic assessment of FTOs [8] has received scant attention despite being an important factor from the point of durability for lifetime device performance as well as during processing and packaging. The two important parameters, elastic modulus and hardness studies by nanoindentation experiments provide information about the elastic deformation and resistance to permanent deformation properties of the thin films. To ensure longevity, robustness and good reliability of modern electronic devices, wear-resistant properties of FTO coatings become essential. Herein, we exploit a production-type APCVD process with in-line configuration to deposit FTO films of various fluorine doping levels (through flash evaporation of aqueous trifluoroacetic acid solution) and multiple thicknesses. We firstly describe nanoindentation experiments performed on the FTO films to assess their mechanical behaviours at the nanoscale level in this paper, which is the first such type of published study on high throughput APCVD deposited FTOs.

Secondly, to help elucidate and compare the optical properties between the different FTO morphologies this paper will focus on various angle spectroscopic ellipsometry (SE) measurements. The optical properties are of particular importance for TCO's used within solar cells as the device performance is directly affected by the amount of light reaching the absorber layers and its efficient exploitation. For example various groups [9] have performed SE studies of highly textured FTOs because of enhanced light scattering properties at the interface which is of

particular advantage for silicon-based solar cells where the absorber is relatively poor so increased use of the incoming sunlight via total internal reflection of light should improve the cell efficiency. Conversely, for perovskite solar cell technologies with an excellent light absorber and rough surfaces are considered to be a disadvantage as it can lead to non-uniform or non-continuous absorbing and/or blocking layers resulting in shunting of solar cells [10]. Hence, we will discuss the SE measurements and compare between the optical parameters of FTO thin films of various architectures created by specific processing conditions.

2 Experimental Procedures

All the chemicals acquired from Sigma Aldrich were used without any further purification. 1.1 mm Borosilicate glass substrates (10 × 10 cm) were cleaned with detergent, water, 1-propanol, and dried in air.

Before commencing, the heated APCVD gas delivery system was flushed with nitrogen for approximately 2 hours to remove any moisture or contaminants. Monobutyltin trichloride (MBTC) and aqueous trifluoroacetic acid (TFAA) solution (0.2, 0.6 and 1M) were delivered with a Sn precursor to H_2O molar ratio of 1:5. MBTC was vaporized at 123 °C (carrier gas = 0.6 L min^{-1}) and aqueous TFAA solution was flash evaporated (carrier gas = 0.7 L min^{-1}). The carrier gas composed of N_2 diluted with 15% oxygen (total flow = 1.5 L min^{-1}) was fixed throughout the coating experiments. A heated susceptor at 600 ± 10 °C was translated under the static CVD head in an extracted and open atmosphere. The number of passes of the susceptor under the coating head was fixed at 4, 6 or 8 to give samples of different thickness. A summary of the experimental conditions is given in Table 1.

X-ray powder diffraction measurements were performed on a Bruker D8 using Cu Kα radiation (λ = 1.5406 Å) with locked coupled measurements taken between 20 – 70° 2θ range with a step size of 0.04. Surface morphologies were recorded using a field emission scanning electron microscope (Lyra3, Tescan) with an accelerating voltage of 20 kV. The surface roughness was determined by atomic force microscopy (NanoScope IIIa, Digital Inst. Ltd., Santa Barbara, California, USA) over a 5 x 5 μm area. The analysis was carried out using Si tips in tapping mode. The tips (NT-MDT Ltd) had a radius of curvature less than 10 nm and a cantilever resonant frequency of around 190 kHz. The film thickness was calculated using a Dektak 3ST surface profiler (Veeco, Santa Barbara, California, USA) where films were step etched using zinc powder and dilute hydrochloric acid.

The ellipsometric data were obtained using a J.A. Woollam Company VASE ellipsometer with its Completease software for the data analysing and modelling. By using the ellipsometry,

we can determine three parameters, FTO film thickness, refractive index (n) and extinction coefficient (k). The ψ (the ratio of the amplitude diminutions) and ∆ (the phase difference induced by the reflection) measurements were done at an incident angle of 65 ^{o} over the spectral range 300 - 1700 nm (0.73 - 4.13 eV). It should be noted that the measurement of the ψ and ∆ at three angles are valuable but adding experimental measurement such as intensity transmission measured independently of ψ and ∆ can help to determine the unique optical model. It is possible to model the FTO refractive index the top and the bottom of the film by using four oscillator (Lorentz oscillators). The thickness is separated into several sublayers of equal thickness. The Bruggeman effective medium approximation (EMA) [11,12] were used to fit the layers including the glass substrate, the FTO film and voids.

An Aquila nkd 8000 spectrophotometer was used for some additional simultaneous measurement of transmission and reflection (350 - 1000 nm) under p polarisation at an incident angle of 30°. Nanoindentation tests were carried out with a nanoindenter (Model: CSM Instruments) capable of imparting small loads (ranging from 0.5 to 300 mN) that enable small volume penetrations. A precise, rigid and sharp Berkovich diamond tip (with three-faced pyramid geometry and tip size of a few tens of nm) was used for these tests. The nanoindenter tip was pressed into the sample at a fixed load and speed. Indentation was performed at loads of 1, 3, 5, 10, 15 and 20 mN and at a load/unload speed of 2 mN/min. Use of different loads allowed for the acquisition of indentation data from various penetration depths. The indenter was held at maximum load for 10 seconds between each loading and unloading phase. Applied normal load and precise depth of penetration (displacement of indenter) were measured continuously throughout the indentation process. These values were plotted in a graphical format to obtain load-displacement curves. Known geometry and size of the indenter tip permits calculation of the area of the indent without the need to visualize it.

Various analytical models are available to obtain hardness, modulus, creep and other mechanical properties i.e., Oliver and Pharr method, [13,14] the deformation energy method, [15-17] the force indentation function method, [18-20] the Joslin-Oliver method, [21,22] and the energy density method [23]. Most popular method is Oliver and Pharr method which was also used for this study. Nanoindentation hardness (*H*) is the resistance to permanent deformation under perpendicular stress and was calculated as follows:

$$H = \frac{P_{max}}{A_p} \text{ Pascals} \qquad \text{eqn. 1}$$

where P_{max} = Maximum load and A_p = Projected contact area

Elastic modulus (E) of the sample was calculated as:

$$E = \frac{1-{v_s}^2}{\frac{1}{E_r}-\frac{1-{v_i}^2}{E_i}} \quad \text{eqn. 2}$$

where E_i = Elastic modulus of the indenter, E_r = Reduced modulus of the indentation contact, v_i = Poisson's ratio of the indenter and v_s = Poisson's ratio of the sample.

The following relationship was used to calculate creep (Cs) as a percentage:

$$C_s = \frac{h_t - h_{max}}{h_{max}} \quad \text{eqn. 3}$$

where h_{max} = displacement at maximum load and h_t = displacement at maximum load after a specified time period

The degree of elastic recovery (R) can be calculated as follows:

$$R = \frac{h_{max} - h_f}{h_{max}} \quad \text{eqn. 4}$$

Where h_{max} is the displacement at maximum load and h_f is the displacement after the load is removed.

The hardness and elasticity data was acquired from the real-time normal load versus penetration depth curves recorded by the computer. A set of four indentations was obtained for each test.

3 Experimental results and discussion

This section is divided into 3 main parts. Firstly, a survey of the FTO thin film material properties, a nanoindentation study and a discussion of the optical properties.

3.1 Material characterization

X-ray powder diffraction measurements (Fig. 1) conclusively confirmed the formation of high polycrystalline tetragonal SnO_2 (JCPDS*:* 00-046-1088*)* without any indication of impurities, for example, Sn or SnO. One notable feature of the X-ray studies was the degree of preferred orientation along the (200) plane which increased with the film thickness. Changing the TFAA concentration has no profound impact on the degree of orientation. Irrespective of TFAA concentration or film thickness, calculated particle sizes only vary between 32-36 nm. This intense (200) peak in the films can be likened to the formation of halogen rich polar molecules during the reaction that adsorb on the polar F-

(101) face [24]. The net result is that it promotes the growth along the (200) plane at the expense of the (100) plane.

From the scanning electron microscope (SEM) studies (Fig. S1), the pyramidal type features having textured grain boundaries dominate for all the films except for 7A. For 7A, the morphology is largely dominated by randomly orientated compact features. From the images, particle sizes increased with film thickness contributing to rougher films. As can be seen the thinnest samples (56A, 28A) showed the smallest grain sizes. Irrespective of morphology, the deposited films are continuous and dense, without any noticeable voids. From the step-etched sample analysis, film thicknesses increased linearly with the number of passes. Using root mean square (RMS) analysis of AFM images, it became obvious the film roughness increased with film thickness. This was mirrored by a reduction in sheet resistance (for fixed dopant level) (Table 1). For a given number of passes, no change (within the experimental error) in either roughness or thickness is evident with varied TFAA concentration (Table 1).

The reduction in sheet resistance with increased film thickness has been previously highlighted by us [25] and demonstrated that this relates to an increase in grain size [26]. The increased grain size in turn reduces the number of grain boundaries and hence traps for electron free carriers so increasing the mean free path and hence mobility [27].

3.2 Mechanical Properties

Accurate assessment of mechanical properties of thin coatings is complicated due to contribution from the underlying substrate. Conventional techniques are not suitable for measuring hardness of thin films due to its use of relatively heavy loads and large indenters. Nanoindentation employs micron-sized indenters that apply small loads in the order of few mN, which serve to analyze only small volumes of materials. This allows assessment of coating's response to indentation without contribution from the underlying substrate material. The rule of thumb is to keep the penetration depth of the indent to 10% of the coating thickness to preclude influence of the substrate. On the other hand, small penetration depths result in small indent size that might be comparable to sample surface roughness. This will introduce an error in measurement. To avoid such as error, the recommendation is to indent at a larger depth i.e., at least 20 times the arithmetic roughness of the surface, such that the roughness is less than 5% of penetration depth. Usually, a compromise has to be achieved between these two competing conditions. When coating thickness is very small i.e., few tens or hundreds of nanometer, accurate

assessment of hardness becomes complicated. For soft films on hard substrates, hardness values will show an increase with increasing penetration depths of the indenter. For hard films on soft substrates, hardness will decrease with increasing penetration depths. If a material is truly elastic, the unloading curve traces back the loading curve leaving behind no indent. If the material is fully plastic, there is no recovery and the unloading curve falls straight down. Most materials will show elastic and plastic regimes. The area between the loading and unloading curves represents the plastic regime. The area outside of the unloading curve indicates the elastic regime.

The thickness of the FTO coatings ranged from 370 to 750 nm as shown in Table 1. Typical plots obtained from nanoindentation test of FTO coatings are shown in Fig. S2. The applied normal load and displacement (penetration depth of the indenter) are shown plotted versus time in Fig. S2(a). The normal load versus penetration depth for the same indent is plotted in Fig. S2(b). These curves are used to calculate mechanical properties of the coatings using Oliver & Pharr method. Four indents were made at different locations on the surface of each sample. The plotted values are an average of four load-displacement curves generated at each load.

Nanoindentation of each coating sample was carried out at loads of 1, 3, 5, 10, 15 and 20 mN. The superimposed load-displacement curves obtained from each sample at various loads are shown in Fig. 2 a-j. It can be seen, as expected, that the penetration depth increases as the load is increased for all coatings. Fig. S3 shows superimposed load-displacement curves obtained from sample of glass, 56A, 19A, 28A, 34A, 14A, 10B, 10A, 7A and 24A at normal loads of 1, 3, 5, 10, 15 and 20 mN, respectively. It can be seen that the penetration depth increases consistently with normal load for all samples.

Fig. S4 demonstrates the relationship between penetration depth and load for each sample in the form of a bar chart. All samples were loaded at a fixed rate of 2mN/min. Due to small thickness of coatings used, the penetration depths of the indenter was more than the recommended 10% for all samples.

Fig. 3 shows the relationship between the normal load and nanoindentation hardness for each coating in the form of a vertical bar chart. The nanoindentation hardness of all coatings was within the range of 8-20 GPa. At low loads (e.g., 1 - 3 mN) and penetration depths, accurate measurement of hardness is made complicated due to transition from purely elastic to elastic/plastic state of the indented region [13]. Small size of the indent is more likely to be influenced by the surface roughness of the sample. The instrument is also working close to its sensitivity limit. At medium loads, the contribution from the

substrate is small and the values are more representative of true hardness of the coatings. At higher loads, the influence of the glass increases and results in lower hardness values for the coatings. For all coatings, a plateau in the hardness (at 3 - 5 mN loads) was observed which is typical when hard coatings deposited on soft substrates are subjected to nanoindentation [22,28]. At shallow displacement, where total indentation depth is much smaller than the film thickness, the effect of substrate was not present. At these small depths, increase in hardness was observed due to plastic strain gradient hardening in the film present between the indenter and the substrate [26].

The hardness decreased with increasing loads from that point onwards indicating that the glass substrate yielded at indentation depths much less than the film thickness. For such a case, where a hard film is deposited on a soft substrate that yields early during indentation, the rule of thumb of film thickness being less than 10% of indentation depth becomes important. At still higher loads, the hardness of all coatings decrease and converge toward the hardness of the glass, whose contribution becomes more evident as penetration depths increases. However, the indentation hardness never becomes a constant even after the indentation depth reaches the film thickness (for samples 56A and 19A). This phenomenon is typical of a hard coating on a soft substrate and is in contrast with the behaviour shown by a monolithic material [29].

It is noted that at the highest load used (e.g., 50 mN), the hardness of the thicker coatings is still high due to a lesser influence of the substrate effect. The glass did not exhibit a large variation in hardness at various loads signifying behaviour of a monolithic material. Its average hardness value was 9.34 GP. A good estimate of nanohardness of coatings is likely to be the average hardness value at the plateau formed at 3-5 mN loads. Sample 7A exhibited the highest hardness at these load values. There was no evidence of correlation between the hardness and thickness of coatings at a given displacement. For similar structure and constitution of a hard coating on a soft substrate, the coating with a higher thickness would exhibit higher hardness at a given indentation depth. Such a correlation was not observed in this study indicating the probable role of coating constitution and/or structure in defining the surface mechanical properties of coatings.

Fig. 4 shows values of elastic modulus (E) plotted against normal load used for each coating sample. The elastic modulus decreases continuously with increasing normal load and approaches that of the underlying glass substrate. The elastic modulus of all the FTO thin films is greater than that of glass and reaches the lower values reported for bulk FTO. Irrespective of the orientation, the reported E values for tin oxide vary between 174-368

GPa [30,31]. The elastic modulus of glass is approximately 63 GPa. Large mismatch in the modulus of the film and glass substrate makes it difficult to measure the film modulus accurately as the long-range elastic field under the indenter extends into the substrate.[22] This effect is higher in films of small thickness. In this study, at any given load, the modulus generally increased slightly with coating thickness. This indicates larger influence of the underlying soft substrate to the modulus in coatings with small thickness.

Hardness to modulus (H/E) ratios of solid films can be used as a means to ascertain their mechanical integrity [32-35]. Fig. 5a shows the values of H/E plotted against normal load for each coating sample. It can be seen that H/E values vary within a small range at various loads and remain comparable for all coatings. The variation in H/E values is small for all coatings indicating comparable mechanical/tribological capability.

For each load-displacement plot, the load was kept constant at its maximum value for 10 seconds before unloading was initiated. At constant load, increase in penetration depth was observed indicating plastic deformation of coating through the phenomenon of creep. The values of creep obtained are plotted for each coating at various loads used in Fig. 5b. The mean values of creep ranged between 1.5-2 % for all samples. The degree of elastic recovery for each coating is plotted in Figure 5c. It can be seen that average values of elastic recovery for all coatings lie between a small range of 45-50%. This is consistent with the findings found in the literature [36]. The elastic recovery is largely not influenced by thickness of the coatings or the applied normal loads.

3.3 Optical properties

The spectroscopic ellipsometry data in Fig. 6 show ψ and Δ fit over the spectral range (300 – 1700 nm). It is evident that there is a good agreement between the experimental and the modelled data. However, there is a small deviation in the ψ and Δ fitting, which is largely due to surface variations for example, roughness, and grain boundaries along with the film thickness. In fact, this kind of deviation occurs due to the depolarization of the incident light caused by the presence of the grain boundaries and the roughness of the front surface, in addition the rough surface of the backside of the film. As shown above that the film thickness is dependent on the number of passes. Again, the SEM images of films confirm particles sizes between 400-700 nm with pyramidal structural features.

Fig. S5 shows the fitting of the optical refractive constant (n) and extinction coefficient (k) at the top and the bottom of the film. It was noted that the extinction coefficient is lower nearer the substrate-film interface than the top surface. This is possibly due to the film being more conductive near the surface, suggesting that the film is denser at the top. This

consequently induced an enhancement of the conduction due the continuous film at the interface. Synowcki et al. reported a similar observation for indium tin oxide films [37,38] Increased surface conductivity could also relate to a higher F concentration at the surface due to species migrating within the FTO during deposition. This was previously reported by Manceriu et al. [39], although with APCVD films that had been quenched. Normally, the surface characteristics in particular, roughness and grain boundaries greatly affect the reflectance, i.e. the intensity of the reflected light is affected by the films morphology. In this case, the thinnest and hence smoothest FTO films, 56A (RMS = 13 nm), 28A (RMS = 12 nm), and 19A (RMS = 13 nm) would be expected to show higher reflection, as less light will be scattered. These samples have a homogeneous surface with reduced roughness (Fig. S1 and S6).

From Fig. S5, it is evident that the films have a similar variation of the extinction coefficient, depending on the wavelength of the polarized light. The k values are very small at the higher wavelength region i.e. 600 - 900 nm, where the films are almost transparent. Although there is an increasing difference between the top and bottom k values at higher doping levels (for each set of film thicknesses), which may relate to an increase in free carrier absorption.

Ellipsometry results summarised in Table 2 show the calculated film thicknesses are very similar to ones obtained from the surface profilometer. Generally, the refractive index of a bulk material is higher than that of a thin film due to a variety of properties including lower stresses during formation, which can lead to larger crystallite sizes and lower number of grain boundaries. This is seen with our results with n between 1.64 and 1.86 opposed to 2.006 for bulk crystalline tin IV oxide [40]. As can be seen in Table 2, the level of doping does have an effect with a general decrease in n with an increase in the precursor dopant concentration for particularly the thinner samples. This is in agreement with earlier work from Afify et al [41]. Also seen (particularly for the FTO samples doped with 0.6 M and 1.0 M TFAA) was a decrease in average refractive index as the films increased in thickness. An increase in the number of passes relates directly to an increase in film thickness and surface roughness. The higher thickness samples are rougher so give a graded interface between the air (n = 1) and the FTO film, so that there is a gradual refractive index change to a slightly lower value.

There is a clear link between increasing refractive index and density [42], so a reduction in n should relate to decreasing film density (increasing porosity). Volume porosity estimations from the refractive index values (wavelength 633 nm) confirmed this trend.

This was particularly clear for the 0.6 M TFAA doped samples with a relative change in porosity from 25% for the thinnest sample (28A), 39% (14A) to the thickest at 43% (10A). These values are not absolute, as they assume the bulk n value is for completely dense tin IV oxide and that there is no effect from the doping level.

These were based on the Lorentz-Lorentz relationship as described by Fallet et al [43], along with the bulk SnO_2 value.

$$1 - \frac{P}{100} = (n^2 - 1)/(N^2 - 1) \times (N^2 + 2)/(n^2 + 2) \quad \text{eqn. 5}$$

The bandgap of a material is generally affected by the concentration and type of dopant, so the ellipsometry derived k values were used with the equation below [44] to obtain the absorption coefficient and hence via Tauc plots an estimation of optical bandgap.

$$\alpha = 4\pi k/\lambda \quad \text{eqn. 6}$$

The values extracted from Tauc plots (See Fig. S7) are subject to some various as the exact value will depend on exactly which points are considered to be in a straight line. For all samples an optical bandgap of about 4.7 eV was obtained, which confirmed that doping has taken place as undoped, pristine SnO_2 has a bandgap of 3.7 eV. The shift in bandgap, although high, is in line with that seen for FTOs by other researchers [45].

To validate the fitted ellipsometry values a comparison of the thickness and refractive index measurements extracted from the SE measurements were also compared with selected independent results derived from transmission and reflection measurements. These results were in excellent agreement with both SE and physical surface profile measurements.

The FTO films all showed strong interference fringes as shown in Fig. S8 The wavelength position of the maxima and minima of these can be used to extract values for film thickness, as well as refractive index at specific wavelengths. There are several methods available that each have their own advantages and disadvantages. These all stem from the basic equation for interference fringes

$$2nd = m\lambda \quad \text{eqn. 7}$$

where m is an integer for maxima, n is the refractive index, d thickness of film and λ wavelength. However, use of this equation requires knowledge of either n or d. The first method applied calculates the product of thickness and refractive index, nd, from either transmission or reflection. It was also possible to allow for the angle of incident light [46] which was 30° within the spectrophotometer used. The calculated values of the nd product

were, within experimental error, identical for both reflectance and transmission. To determine the actual thickness a refractive index value from the ellipsometry was used. This was chosen to be midway in the wavelength range used for the nd calculation.
The thickness of a film, d, is given by

$$\mathrm{d} = \frac{\Delta m}{2\sqrt{n^2 - \sin^2\phi}} \cdot \frac{1}{\left(\frac{1}{\lambda_1} - \frac{1}{\lambda_2}\right)} \qquad \text{eqn. 8}$$

where ϕ is the light incident angle, λ_1 and λ_2 are the peak or valley wavelengths in the spectrum and Δm is the number of peaks or valleys between λ_1 and λ_2. So a plot of number of the maxima (integers) and minima (1/2 integers) against reciprocal wavelength will give a gradient as given in eqn. 9 and hence a value for film thickness or refractive index.

$$\text{gradient} = 2d\sqrt{n^2 - \sin^2\phi} \qquad \text{eqn. 9}$$

The second way of calculating these values was by use of the envelope method which was originally proposed by Manifacier et al. [47] and later developed by Swanepoel [48].

$$\mathrm{n} = \left[N + (N^2 - n_S^2)^{\frac{1}{2}}\right]^{\frac{1}{2}} \qquad \text{eqn. 10}$$

when N is

$$\mathrm{N} = 2n_S \frac{T_M - T_m}{T_M T_m} + \frac{{n_S}^2 + 1}{2} \qquad \text{eqn. 11}$$

T_M and T_m are the maxima and minima transmission values and n_s the refractive index of the substrate.
Subsequently calculating thickness using

$$d = \frac{\lambda_1 \lambda_2}{2(\lambda_1 n_2 - \lambda_2 n_1)} \qquad \text{eqn. 12}$$

It is only possible to use transmission measurements for this and other research studies assumed a fixed refractive index for the substrate [49]. In our studies use of a wavelength dependent refractive index for the substrate made little change to the resulting refractive index and hence thickness values.

Using the method (Method 1) defined by eqn. 8 and 9 there was excellent agreement (within experimental error) between the physical surface profiler film thickness

measurement and that calculated by this method. See Table S1. The ellipsometry derived values were also close and differing no more than 1%, although fractionally higher. All these methods gave much higher values than those obtained by the envelope method. The increased difference of thickness with the envelope method (Method 2) is probably to be expected as the errors will be greater as could only be determined indirectly from a maximum of three calculated refractive indices in each case. In addition, eqn 12 is very sensitive to errors in n and hence not very accurate [48].

The calculated film refractive index values via the envelope method all showed the correct trend of increasing n against decreasing wavelength, within each set of doped samples. See Table S2. A similar trend was seen over all samples, although with some exceptions due to the different levels of F-doping.

All these values are 1% to 2% lower than the equivalent ellipsometry refractive index values. This relates, in part, to the use of a fixed substrate refractive index of 1.505. Use of a larger value of ns although it would increase the film refractive index would reduce the calculated film thickness, which is already less than expected.

Overall, ellipsometry has the advantage of providing film thickness and refractive index over the full wavelength range, while use of less sophisticated instrumentation and calculations is capable of giving excellent thickness agreement (Method 1) and reasonable values for refractive index (Method 2) at specific wavelengths. However, the latter methods do depend on the presence of strong interference fringes from the thin film samples.

4 Conclusions

We have attempted to develop an understanding of mechanical and optical properties of (200) orientated FTO thin films produced by in-line APCVD process through nanoindentation and ellipsometry measurements. A general increase in the modulus was noted as the films became thicker. It was found that hardness ranged from 8 to 20 GPa. To validate the ellipsometry derived refractive index and thickness values, independent optical data was also found to be similar.

Compliance with ethical standards

Conflict of Interest The authors declare that they have no conflict of interest.

Acknowledgements

This work was part financed by EU Horizon 2020 grant H2020-LCE-2015-16-53296 CHEOPS Highly Efficient Photovoltaic Perovskite Solar Cells.

References

1. (a) C, Beneking, B, Rech, S. Wieder, O. Kluth, H. Wagner, W. Frammelsberger, R. Geyer, P. Lechner, H. Rubel, H, Schade, Thin Solid Films **351,** 241 (1999); (b) W.-H. Baek, M. Choi, T.-S. Yoon, H.H. Lee, Y.-S. Kim, Appl. Phys. Lett. **96**, 133506 (2010); (c) A. Way, J. Luke, A.D. Evans, Z. Li, J.-S. Kim, J.R. Durrant, H.K.H. Lee, W.C. Tsoi, Appl. Phys. Lett. **9,** 085220 (2019); (d) J.D.Benck, B.A. Pinaud, Y. Gorlin, T.F. Jaramillo, PloS one **9**, e107942 (2014); (e) A. Urbina, J. Phys. Energy **2,** 022001 (2020); (f) A. Korjenic, K.S Raj, J. Electrochem. Soc. **166**, 6 (2019); (g) Q. Gao, H. Jiang, M. Li. P. Lu, X. Lai, X. Li, Y. Liu, C. Song, G. Han, Ceram. Int. **40** 2557 (2014).
2. H.M. Yates, M. Afzaal, A. Walter, J.L. Hodgkinson, S.-J. Moon, D. Sacchetto, M. Bräuninger, B. Niesen, S. Nicolay, M. McCarthy, M.E. Pemble, I.M. Povey, C. Ballif, J. Mater. Chem. C **4,** 11269 (2016).
3. A,-L. Anderson, S. Chen, L. Romero, R. Binions, Buildings **6,** 1 (2016).
4. A.Sandström, H.F. Dam, F. C. Krebs, L. Edman, Nat. Commun. **4,** 1002 (2012).
5. V, Palenskis, J.Matukas, S. Pralgauskaitė, Solid State Electronic **54,** 781 (2010).
6. http://www.mtixtl.com/FTO-252522TEC7-25.aspx
7. (a) Z.Y. Banyamin, P.J. Kelly, G. West, J. Boardman, Coatings **4,** 732 (2014); (b) N. Noor, I.P. Parkin, J. Mater. Chem. C **1,** 984 (2013); (c) M. Afzaal, H.M. Yates, J.L. Hodgkinson, Coatings **6,** 43 (2016); (d) J.H. Park, D. J. Byun, J. K. Lee, J. Electrochem. **23,** 506 (2009).
8. L.T.C. Tuyen, S-R. Jian, N.T. Tien, P.H. Le, Materials **12,** 1665 (2019).
9. For example see (a) J. Isidorsson, C.G. Granqvist, K. von Rottkay, M. Rubin, Appl. Opt. **37,** 7334 (1998); (b) F. Atay, V. Bilgin, I. Akyuz, E. Ketenci, S. Kose, J. Non-Cryst. Solids **356,** 2192 (2010); (c) G. Yuan, K, Wang, M. Li, Q. Gao, Y. Liu, S. Jia, C. Song. G. Han, Mater. Res. Express, **3,** 105048 (2016).
10. M .Afzaal, H.M Yates, A. Walter, S. Nicolay, IEEE J. Photovolt. **9,** 1302 (2019).
11. D.A.G. Bruggeman, Ann. Phys. **416,** 636 (1935).
12. D.E. Aspnes, J.B. Theeten, F. Hottier, Phys. Rev. B **20,** 3292 (1979).
13. W.C. Oliver, G. M. Pharr, J. Mater. Res. **7**, 1564 (1992).
14. G.M. Pharr, Mater. Sci. Eng. A **253,** 151 (1998).
15. B. Rother, D.A. Dietrich, Surf. Coat. Technol. **74–75,** 625 (1995).
16. X. Li, D. Diao, B. Bhushan, Acta Mater. **45,** 4453 (1997).

17. S. Veprek, International Conference on Trends and Applications of Thin Films, TAFT 2000, Nancy, France, March 2000.
18. P. Karvankova, H.D. Manning, C. Eggs, S. Veprek, Surf. Coat. Technol. **146–147**, 280 (2001).
19. C. Friedrich, G. Berg, Thin Solid Films **290–291,** 216 (1996).
20. J. Musil, F. Kunc, Surf. Coat. Technol. **154,** 304 (2002).
21. R. Saha, W.D. Nix, Mater. Sci. Eng. A **319-321,** 898 (2001).
22. R. Saha, W.D. Nix, Acta Mater. **50,** 23 (2002).
23. B. Rother, T. Lunow, G. Leonhardt, Surf. Coat. Technol. **71,** 229 (1995).
24. A. Smith, J.-M. Laurent, D.S. Smith, J.-P. Bonnet, R.R. Clemente, Thin Solid Films **266,** 20 (1995).
25. D.W. Sheel, H.M. Yates, P.Evans, U. Dagkaldiran, A. Gordijn, F. Finger, Z. Remes, M. Vanecek, Thin Solid Films**, 517**, 3061 (2009).
26. U. Mehmood, M. Afzaal, A. Al-Ahmed, H.M. Yates, A.S. Hakeem, H. Ali, F.A. Al-Sulaiman, IEEE J. Photovol. **7**, 518-524, (2017)
27. H.Z. Asl, S.M. Rozati, Applied Physics A **125**, 689 (2019).
28. S. Chen, L. Liu, T. Wang, Surf. Coat. Technol. **191,** 25 (2005).
29. F. Zhang, R. Saha, Y. Huang, W.D. Nix, K.C. Hwang, S. Qu, M. Li, Int. J. Plast. **23,** 25 (2007).
30. H. Li, R.C. Bradt, J. Am. Ceram. Soc. **74,** 1053 (1991).
31. S. Barth, C. Harnagea, S. Mathur, T. Rosei, Nanotech. **20**, 115705 (2009).
32. A. Leyland, A. Matthews, Wear **246,** 1 (2000).
33. J. P. Gao, W.D. Luedtke, U. Landman, Science **270,** 605 (1995).
34. J.C.A. Batista, C. Godoy, G. Pintaude, A. Sinatora, A. Matthews, Surf. Coat. Technol. **174–175,** 891 (2003).
35. B.D. Beake, N. Ranganathan, Mater. Sci. Eng. A **423,** 46 (2006).
36. Q. Gao, H. Jiang, M. Li, P. Lu, X. Lai, X. Li, Y. Liu, C. Song, G. Han, Ceram. Int. **40,** 2557 (2014).
37. R.A. Synowicki, Thin Solid Films **313–314,** 394 (1998).
38. H. El Rhaleb, E. Benamar, M. Rami, J.P. Roger, A. Hakam, A. Ennaoui, Appl. Surf. Sci. **201,** 138 (2002).
39. L. M. Manceriu, A. Maho, C. Labrugere, E. Tixhon, A. Schrijnemakers, A. Rougier, P. Colson, R. Cloots, ACS Omega **5** 14999 (2020).

40. P. Pradyot, (2003) Handbook of Inorganic Chemicals, The McGraw-Hill Companies, Inc. p. 940.
41. H.H. Afify, R.S. Momtaz, W.A. Badawy, S.A. Nasser, J. Mater. Sci. Mater. Elec. **2** 40 (1991).
42. M. Ohring, (1992) The Material Science of Thin Films, Academic Press, p. 540.
43. M. Fallet, S. Permpoon, J.L. Deschanvres, M. Langlet, J. Mater. Sci. **41**, 2915 (2006).
44. F. Demichelis, E. Minetti-Mezzettit, V. Smurrot, A. Tagliaferrot, E. Tressoi J. Phys. D: Appl. Phys. **18**, 1825 (1985).
45. (a) A.L. Dawar, J. C. Joshi, J. Maters. Sci **19** 1 (1984); (b) H. Kim, R.C.Y. Auyeung, A.Piqué, Thin Solid Films **516**, 5052 (2008); (c) A.J. Martinez, D.R. Acosta, Thin Solid Films **483**, 107 (2005).
46. F.R. Chowdhury, S. Choudhury, F. Hasan, T. Begum, J. Bangladesh Acad. Sci. **35,** 99 (2011).
47. J.C. Manifacier, J. Gasiot, J.P. Fillard, J. Phys. E: Sci. Instrum. **9,** 1002 (1976).
48. R. Swanepoel, J. Phys. E: Sci. Instrum. **16,** 1214 (1983).
49. M. Caglar, Y. Caglar, S. Ilican, J. Opt. Elect. Adv. Mater. **8**, 1410 (2006).

Table 1 Some properties of deposited FTOs as a function of their processing parameters

Sample No	TFAA concentration (M)	Number of passes	R_s ($\Omega\ \square^{-1}$)	*d* (μm)	*p* (Ω cm)	RMS (nm)
56A	0.2	4	52	0.37	1.94E-03	13
34A	0.2	6	34	0.50	1.69E-03	20
24A	0.2	8	24	0.75	1.79E-03	23
28A	0.6	4	28	0.40	1.12E-03	12
14A	0.6	6	14.8	0.51	7.52E-04	17
10A	0.6	8	10.6	0.72	7.59E-04	21
19A	1	4	19.5	0.38	7.35E-04	13
10B	1	6	10.7	0.55	5.91E-04	21
7A	1	8	7.5	0.73	5.45E-04	25

R_s = sheet resistance, *d* = thickness (via surface profiler), *p* = resistivity

Table 2 Ellipsometry derived thickness and refractive index of films

samples	Number of passes	thickness (μm)	average *n** *(refractive index)*
56A	4	0.338	1.74
34A	6	0.517	1.64
24A	8	0.704	1.71
28A	4	0.351	1.68
14A	6	0.505	1.52
10A	8	0.694	1.48
19A	4	0.372	1.64
10B	6	0.537	1.61
7A	8	0.756	1.57

*Averaged over 300 -1700 nm

Captions

Fig. 1 XRD patterns FTOs using (a) 0.2M, (b) 0.6M and (c) 1M TFAA concentrations. Blue (4 passes), brown (6 passes) and grey (8 passes).

Fig. 2 Superimposed load-displacement curves obtained at normal loads of 1, 3, 5, 10, 15 and 20 mN from sample (a) Glass, (b) 56A, (c) 19A, (d) 28A, (e) 34A, (f) 14A, (g) 10B, (h) 10A, (i) 7A and (j) 24A.

Fig. 3 Bar chart showing the change in nanoindentation hardness with normal load. The nanoindentation hardness of all coatings was within a range of 8-19 GPa. The maximum hardness was achieved at a load of 5 mN for all samples. At higher loads, the hardness decreased with increasing normal load. At high loads, the hardness approached that of the glass substrate, which is relatively soft.

Fig. 4 Elastic modulus (*E*) versus normal load for each coating sample. Elastic modulus decreases with increasing normal load for all samples.

Fig. 5 (a) Plot of *H*/*E* versus normal load for each coating sample. (b) Plot of creep versus normal load for all coating samples. (The variation in creep results for different coatings was small). (c) Plot showing elastic recovery of coatings at various loads. (The effect of coating thickness or applied load on the degree of elastic recovery is not significant).

Fig. 6 Spectroscopic ellipsometry data and fits to Ψ and Δ of thin films at 65 ° for sample (a) 56A, (b) 34A, (c) 24A, (d) 28A, (e) 14A, (f) 10A, (g) 19A, (h) 10B and (i) 7A.

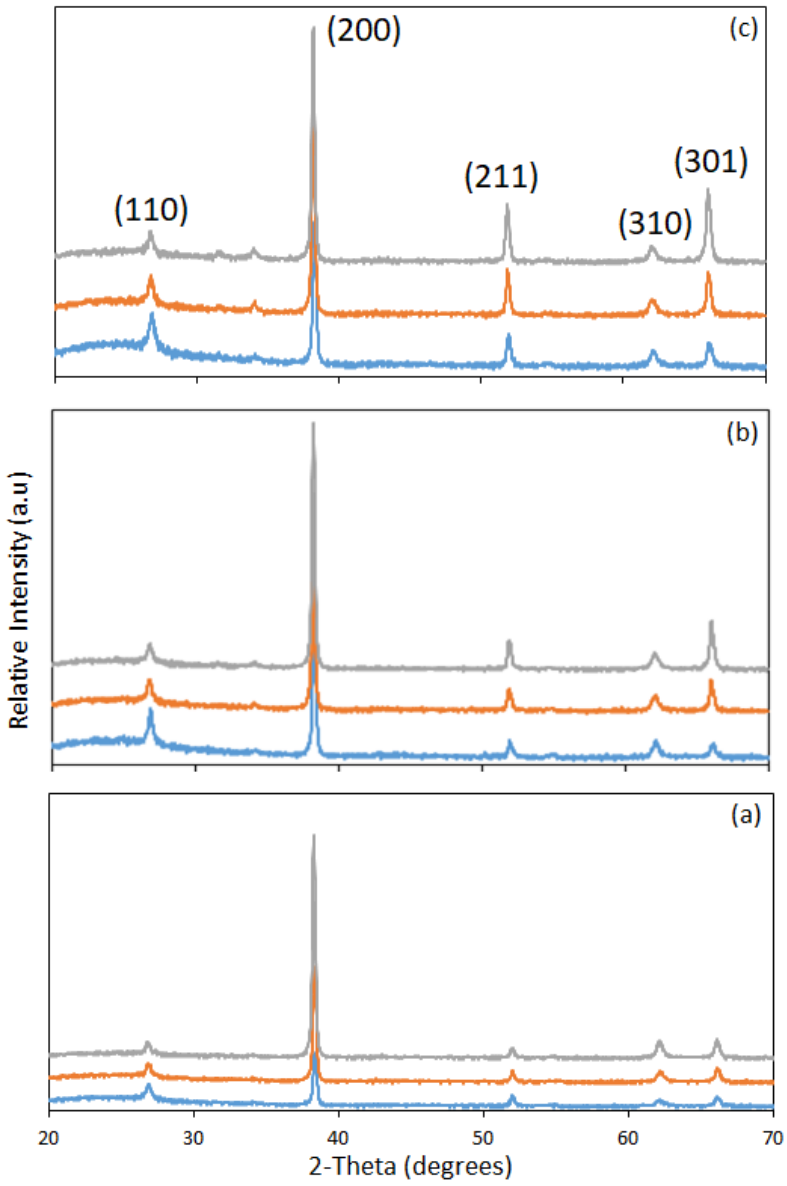
(200)
(c)
(211)
(301)
(110)
(310)
(b)
Relative Intensity (a.u)
(a)
20
30
40
50
60
70
2-Theta (degrees)

Fig. 1

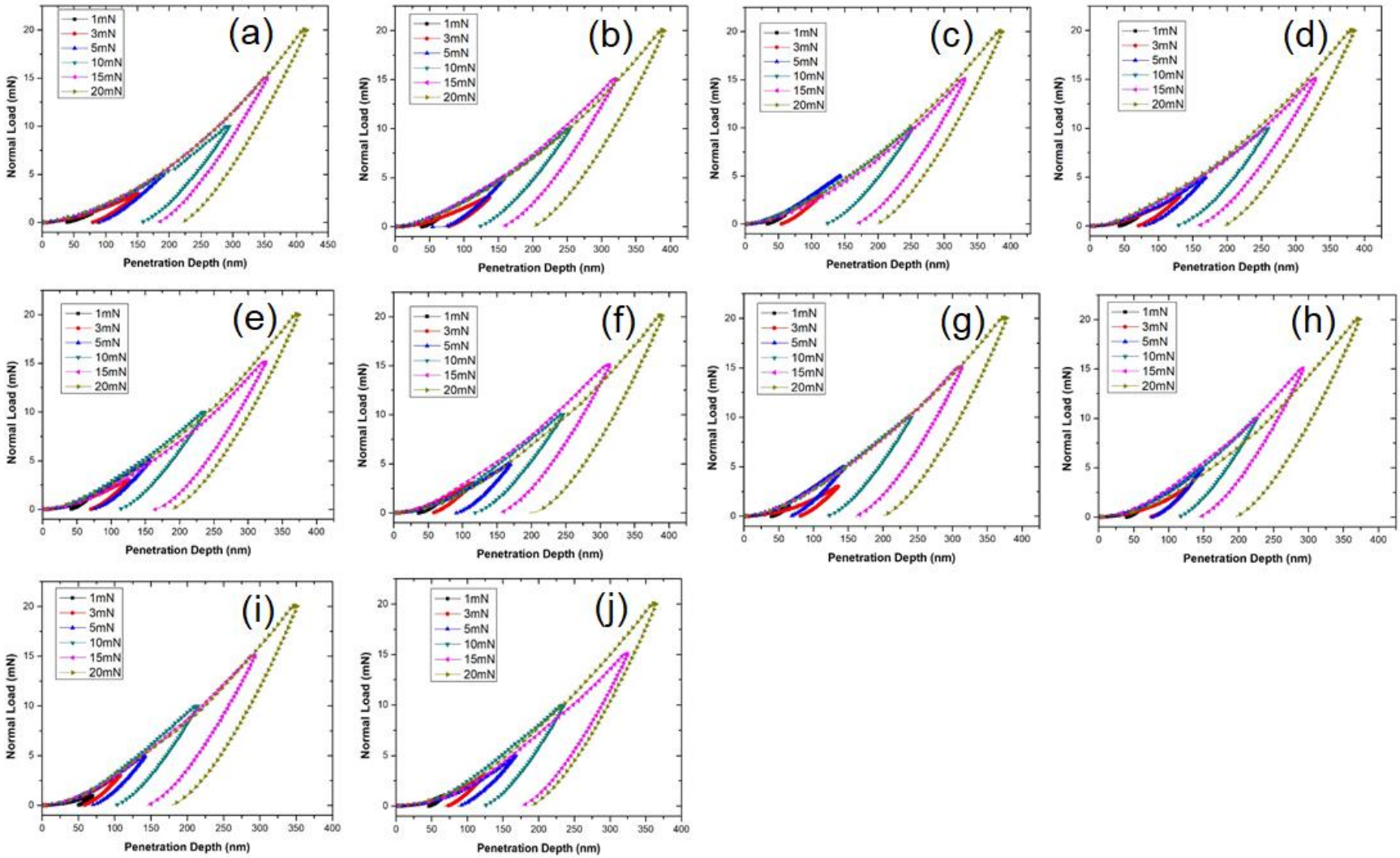
(a)
(b)
(c)
(d)
(e)
(f)
(g)
(h)
(i)
(j)
1mN
3mN
5mN
10mN
15mN
20mN
Normal Load (mN)
Penetration Depth (nm)

Fig. 2

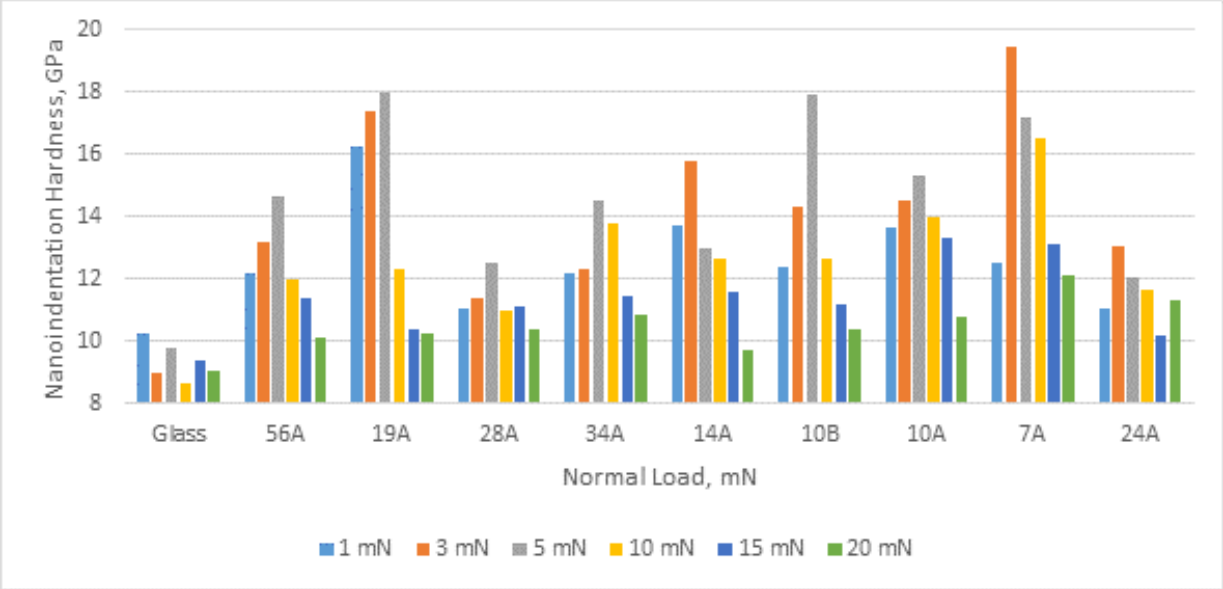
Nanoindentation Hardness, GPa
20
18
16
14
12
10
8
Glass
56A
19A
28A
34A
14A
10B
10A
7A
24A
Normal Load, mN
1 mN
3 mN
5 mN
10 mN
15 mN
20 mN

Fig. 3

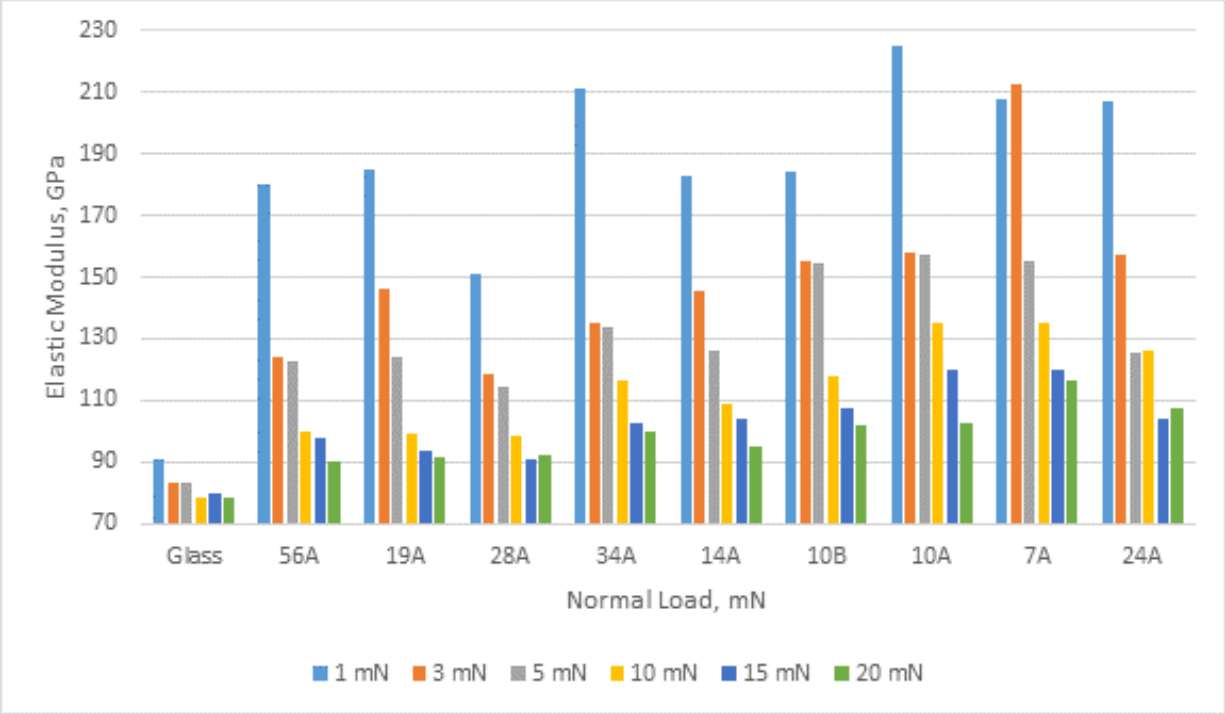
230
210
190
170
150
130
110
90
70
Elastic Modulus, GPa
Glass
56A
19A
28A
34A
14A
10B
10A
7A
24A
Normal Load, mN
1 mN
3 mN
5 mN
10 mN
15 mN
20 mN

Fig. 4

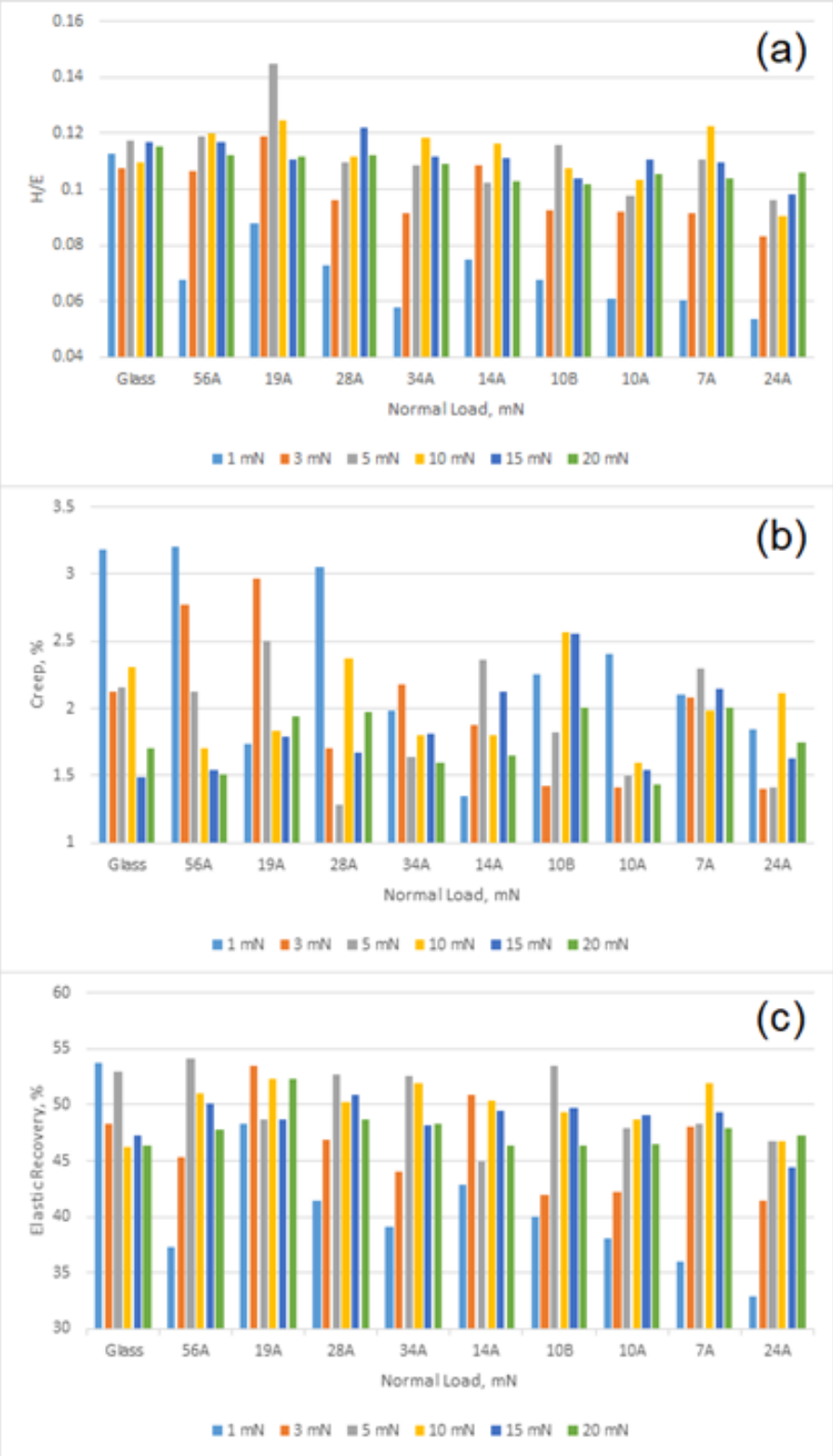
(a)
H/E
0.16
0.14
0.12
0.1
0.08
0.06
0.04
Glass
56A
19A
28A
34A
14A
10B
10A
7A
24A
Normal Load, mN
1 mN
3 mN
5 mN
10 mN
15 mN
20 mN
(b)
Creep, %
3.5
3
2.5
2
1.5
1
Glass
56A
19A
28A
34A
14A
10B
10A
7A
24A
Normal Load, mN
1 mN
3 mN
5 mN
10 mN
15 mN
20 mN
(c)
Elastic Recovery, %
60
55
50
45
40
35
30
Glass
56A
19A
28A
34A
14A
10B
10A
7A
24A
Normal Load, mN
1 mN
3 mN
5 mN
10 mN
15 mN
20 mN

Fig. 5

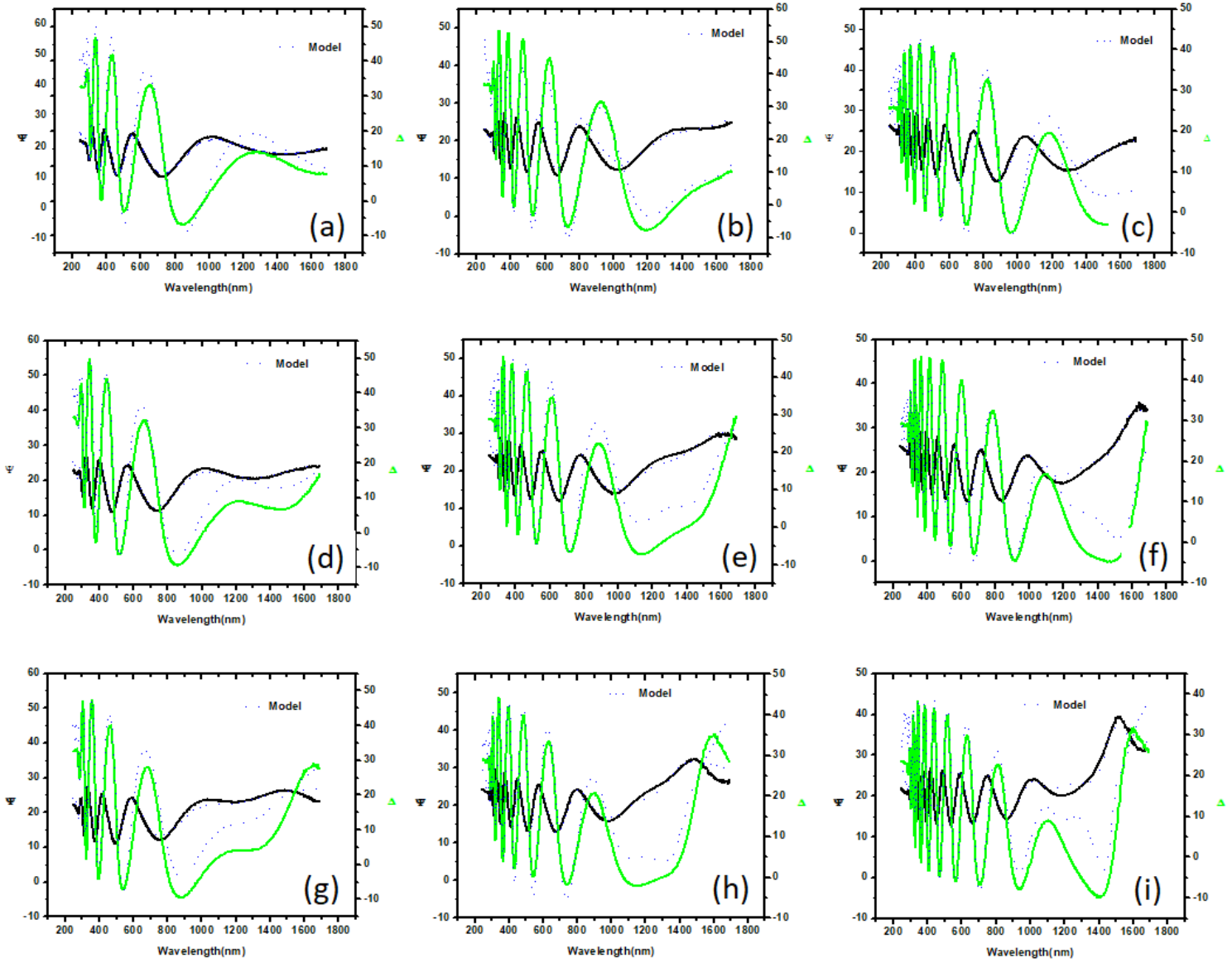

Fig. 6